Élastographie par résonance magnétique du poumon humain

MR elastography of the human lung

Mashhour Chakouch, PhD[1], Fabrice Charleux, MD[2], Philippe Pouletaut, PhD[1], Sabine F. Bensamoun, PhD[1]

[1] Sorbonne University, Université de Technologie de Compiègne, CNRS UMR 7338, Biomechanics and Bioengineering, Compiègne, France, {mashhour.chakouch, philippe.pouletaut, sabine.bensamoun}@utc.fr
[2] ACRIM-Polyclinique Saint Côme, Medical Radiology, Compiègne, France, fabrice.charleux@acrim.fr

RÉSUMÉ. L'élastographie par résonance magnétique (ERM) est une technique d'imagerie non invasive qui est de plus en plus utilisée dans les services de radiologie pour évaluer les différents stades de la fibrose hépatique. Au cours des dix dernières années, de nombreux protocoles ERM ont été développés pour mesurer la rigidité au cisaillement de différents tissus (muscle squelettique, sein, rein, cerveau, …) afin de caractériser le comportement mécanique des tissus vivants. Ainsi, en plus des images anatomiques et texturales obtenues avec l'examen classique en imagerie par résonance magnétique (IRM), il est désormais possible de corréler les caractéristiques morphologiques avec les propriétés mécaniques, permettant un suivi et un traitement plus précis de la pathologie pulmonaire. Pendant la pandémie du COVID-19, l'ERM a trouvé une autre application pertinente dans l'évaluation des dommages au parenchyme pulmonaire résultant d'une infection virale. Cette synthèse bibliographique permet de mieux comprendre l'évaluation par ERM de la biomécanique pulmonaire.

ABSTRACT. Magnetic resonance elastography (MRE) is a non-invasive imaging technique which is becoming more commonly used in radiology departments to assess different stages of liver fibrosis. In the last decade, numerous MRE protocols have been developed to measure the shear stiffness of different tissues such as skeletal muscle, breast, kidney, and brain to characterize the mechanical behavior of living tissues. Thus, in addition to the anatomical and textural images obtained with the classical magnetic resonance imaging (MRI) exam, it is now possible to correlate the morphological features with the mechanical properties, allowing for more accurate follow-up and treatment of lung pathology. During the COVID-19 pandemic, MRE has found another relevant application in the assessment of damage to the lung parenchyma resulting from viral infection. This review provides a better understanding of how to assess pulmonary biomechanics using the MRE technique.

MOTS-CLÉS. Densité pulmonaire, rigidité au cisaillement du poumon, biomécanique pulmonaire, Élastographie par Résonance Magnétique (ERM), module de cisaillement.

KEYWORDS. Lung density, lung stiffness, pulmonary biomechanics, Magnetic Resonance Elastography (MRE), shear stiffness.

1. Context

In 1995, the journal Science published the first paper describing the use of the magnetic resonance elastography (MRE) technique to assess the shear modulus of materials [MUT 95]. The study analyzed the displacement of shear waves inside hard versus soft circular phantoms to determine the variation between wavelengths in both materials. The authors of the study found that magnetic resonance elastography produced a higher wavelength inside the hard tissue compared to the soft one. It is well known that the velocity of a wave is higher through hard media compared to softer media, and from this observation, the objective was to adapt the MRE imaging modality to quantify the stiffness of human biological tissue. Because pathological tissues such as tumor or fibrotic tissues are harder than normal tissue, the MRE technique can therefore be used to diagnose diseases.

Currently, more than 1800 MRE clinical systems are installed around the world with the main clinical application of determining the stage of liver fibrosis. This non-invasive MRE exam has been approved by the FDA and other regulatory agencies all over the world, given that the amplitude of

vibrations produced by MRE within biological tissues is below the maximum amplitude allowable under current standards [EHM 08] (Figure 1).
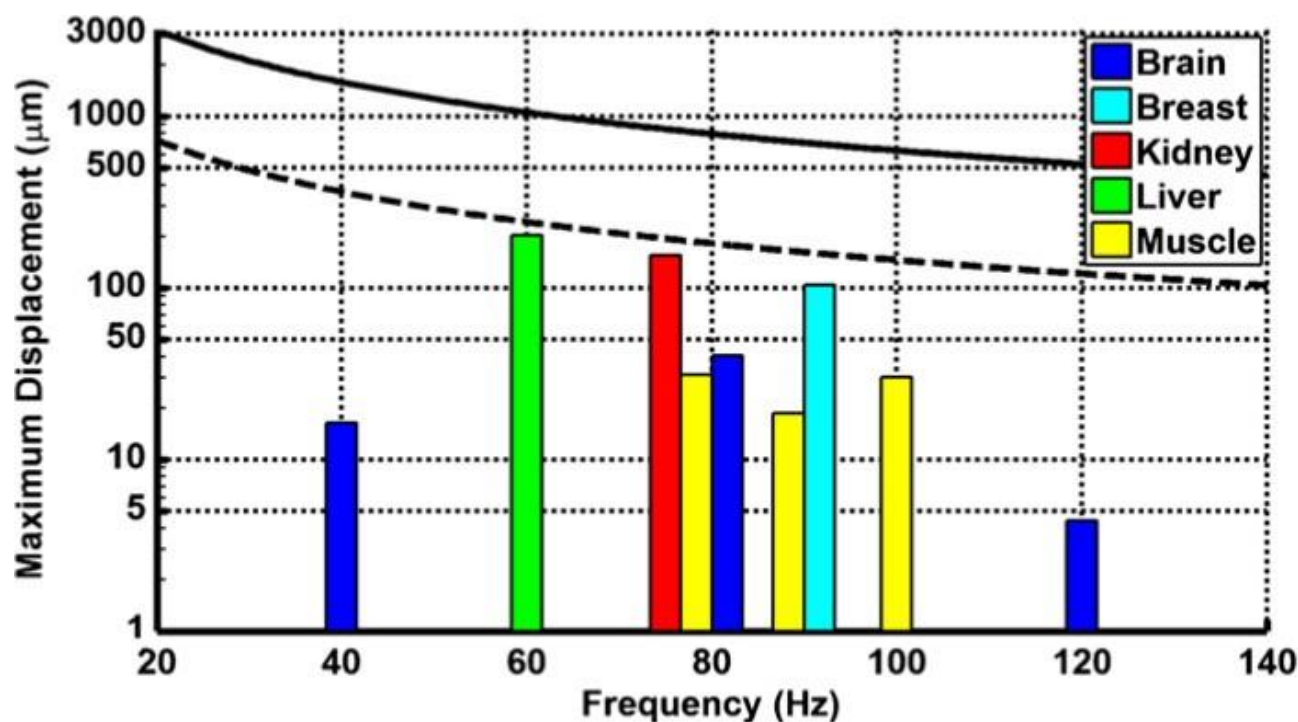

Figure 1. *Maximum tissue displacement authorized by the EU for an exposure of 15 minutes. The dotted line represents the limit for the whole body while the solid line represents the limit for the extremities of the body. The colored bars represent the maximum mean amplitude determined by different MRE systems for different tissues of the human body* [EHM 08].

Currently, shear modulus is the main parameter to assess the mechanical properties of the tissue. In the coming years, however, MRE will be able to assess several additional biomechanical markers (damping ratio, attenuation, etc.) which will be correlated with physiological and structural properties.

While the liver is the first organ approved for clinical MRE analysis, research protocols have been developed to be used for other tissues including brain, breast, kidney, prostate, muscle, lung, heart, disc, pancreas, artery, and cartilage. It is expected that, in the future, the MRE technique will be useful in other routine clinical applications, such as the follow-up of muscle myopathy, the diagnosis of neurodegenerative disease, and others.

In the context of Coronavirus Disease 2019 (COVID-19), the earlier lung damage diagnosis is made, the better the disease management and the patient's chances of survival. The assessment of the lung shear modulus can allow physicians to quantify the biomechanical properties of the lung parenchyma and track these properties over time. This biomarker can be used in conjunction with other forms of data, hereafter described.

2. Anatomy of the lung

The primary function of the respiratory system is to take in oxygen and eliminate carbon dioxide. Inhaled oxygen enters the lungs through the bronchi and travels through narrow bronchioles, which terminate in small alveolar sacs that allow for gas exchange (Figure 2). The alveoli are surrounded by a thin supporting wall, only one cell thick, placing them in very close contact with the surrounding capillaries [NOV 21]. This barrier between air and blood has an average thickness of

about 1 micrometer. Oxygen quickly passes through this barrier and enters the capillary blood. Conversely, carbon dioxide passes from the blood to the alveoli, where it is exhaled.
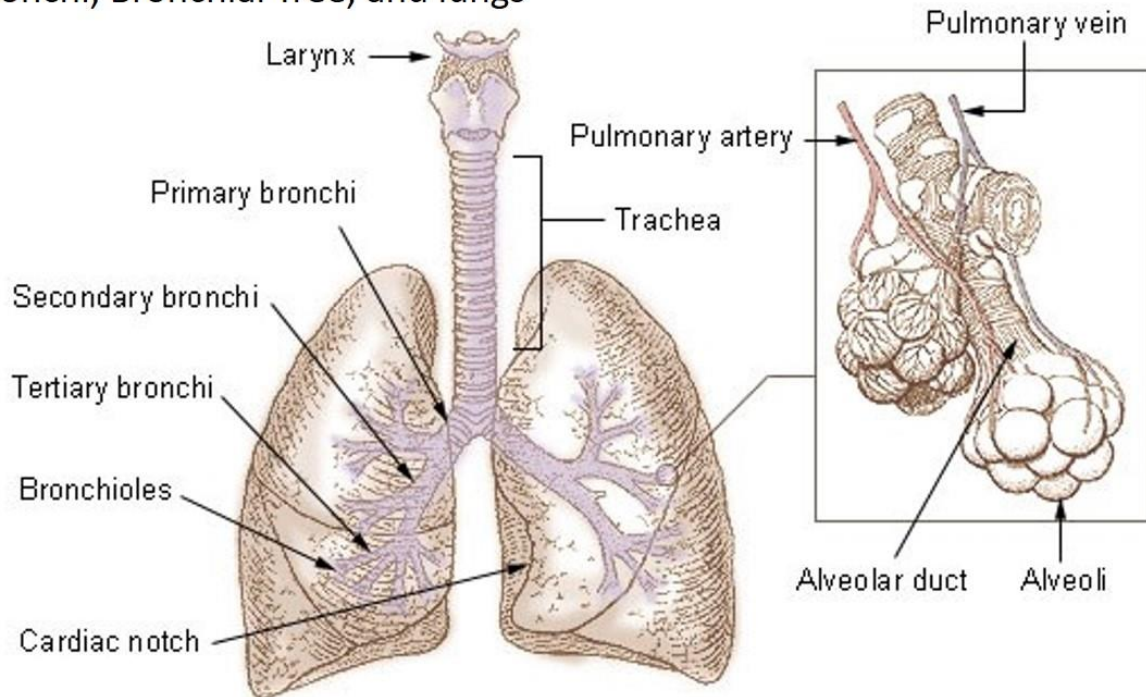

Figure 2. *Lung anatomy (*https://www.physio-pedia.com/Lung_Anatomy*).*

The lung's function is inextricably related to its mechanical behavior, i.e. to its ability to expand and contract [FAF 09]. Aging is strongly associated with gradual changes in declining lung function and respiratory system mechanics [JAN 99], [SHA 06], and several diseases can also impair normal lung activity. Bacterial lung disease is an alveolar syndrome in which the lumen of the alveolar sacs become filled with inflammatory debris. In contrast, viral lung disease is an interstitial syndrome marked by inflammation of the alveolar walls, which may harden and take the appearance of a honeycomb structure [SIC 18], making breathing progressively more difficult. COVID-19 is one example of an acute interstitial syndrome, in which disruptions to lung function can range from mild to life-threatening damage. Other respiratory diseases such as pulmonary hypertension, fibrotic interstitial lung disease (ILD), and asthma also result in progressive architectural and mechanical remodeling of the lung [BUR 16], [HIR 13], [SHIM 13] which negatively affects lung cell function [DIE 17], [LIUF 10], [SHK 15].

3. Computed Tomography

Currently, the detection of pneumopathy is performed by computed tomography (CT) scan (Figure 3), which uses radiation to obtain physiological and morphological data [CHAS 18], [REV 05]. From chest CT scan images, several clinical characteristics can be evaluated such as the volume of the lung parenchyma, the presence of nodules, pleural thickening, airway abnormalities, and underlying lung diseases, such as emphysema or fibrosis. CT scans can also identify ground glass opacities (GGO) and determine their localization and shape (presence of consolidation), the degree of each lung lobe involvement, and the number of lobes affected by GGO [GUA 20], [SHI 20], [WAN 20], [LIUW 20], [DON 21] (Figure 3).

For instance, CT scans from COVID-19 patients can be used to classify disease severity based on the visual evaluation of the GGOs present in inflamed alveolar walls (Figure 3).
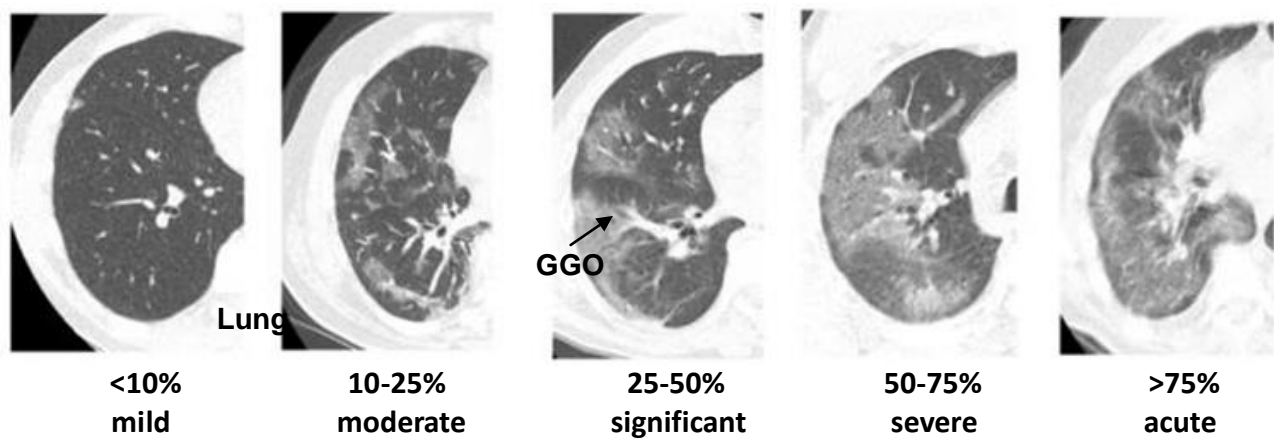
Figure 3. *Classification of interstitial pneumopathy in five grades based on the percentage of ground glass opacities (GGO) (modified image from SFR e-bulletin* https://ebulletin.radiologie.fr/actualites-covid-19/elearning-covid-19-radiologie-z-010420*).*

However, these visual scores from CT scan acquisition are subjective with inter- and intra-operator variability. Further, variable inflation of the patient's lungs at the time of scanning can create inconsistencies, making longitudinal follow-up difficult. Moreover, the imaging analysis takes time, and the diagnosis is often dependent on the experience of the radiologist [CHAS 18].

4. Magnetic Resonance Imaging (MRI)

MRI is not commonly used to examine the lung since the air in the pulmonary parenchyma induces low density and loss of MR signal. Moreover, the anatomical structures (alveoli, blood capillaries) are too small (under 10 microns) for a resonance at a given frequency such that they can be visualized by MRI.

However, a diseased lung will present thicker structures, such as fibrous tissue, that can be identified by MRI acquisition. Indeed, several studies have described recent advances made in MRI with respect to lung cancer. In 2013, Koyama and co-authors published an article reviewing the detection and characterization of solid pulmonary nodules (i.e. lymph node-metastases), staging assessment, prediction of postsurgical lung function, and tumor treatment response. Other MRI research teams have designed magnetic resonance (MR) protocols to measure lung density [THE 09] or magnetic particle concentrations in the lung [SAR 15].

Ultrashort echo time sequences provide morphological information comparable to that of computed tomography. Moreover, MRI can provide not only morphologic information based on various parameters, such as T1 and T2 relaxation times, perfusion, and tissue diffusion, but also functional information (related to respiratory cycle), as radiolabeled aerosols are used in nuclear medicine studies to image lung ventilation [KOY 13], [SAR 14].

In the case of the COVID-19 pandemic, Torkian et al. (2021) have demonstrated the visualization of GGOs, consolidation, reticulation, and a reverse halo sign on multiple MRI sequences [TOR 21]. Ates et al. (2020) have shown similar findings obtained from CT scans of the thorax, which are increasingly used in the diagnosis of COVID-19, and those from MRI acquisition of the lungs, to establish MRI as an important diagnostic alternative [ATE 20] (Figure 4).

In addition to structural and morphological properties obtained with MRI and CT techniques, the elasticity of the lung has been determined *in vitro* [SIC 18] with atomic force microscopy techniques, and Goss et al. (2006) first showed the feasibility of magnetic resonance elastography, or MRE, to quantify lung elasticity *in vivo* [GOS 06].
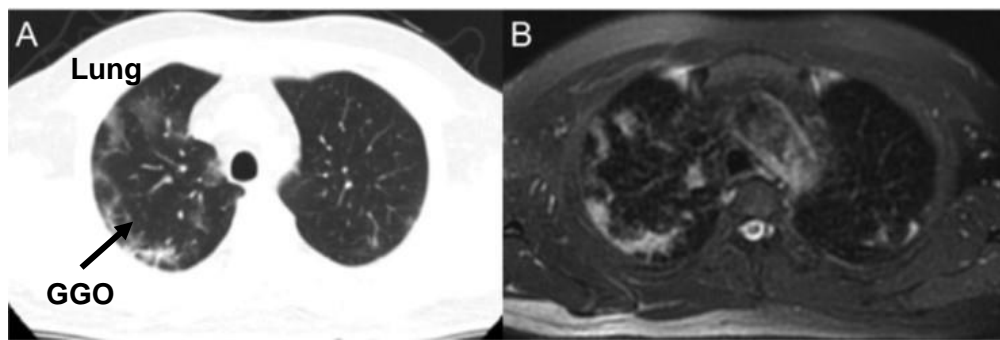
Figure 4. *Ground-glass areas (black arrow) with bilateral peripheral distribution, visualized similarly on both computed tomography (A) and magnetic resonance imaging (B)* [ATE 20].

5. Magnetic Resonance Elastography (MRE)

MRE is a medical imaging technique coupled with (MRI) [MUT 95], [FOW 95] that can non-invasively estimate the mechanical properties of soft tissue in vivo by producing a phase contrast sequence based on shear wave propagation. It is routinely used in clinical practice for the diagnosis of liver fibrosis.

For standard MRI sequences such as Spin Echo (SE), Gradient Echo (GE), Echo Planar Imaging (EPI), and others, a motion-sensitizing gradient (MSG) is imposed in a specific direction and switched in polarity at an adjustable frequency [CAL 95], [DEN 93]. The gradient is synchronized to the local movement of the shear wave, allowing for an increase in sensitivity to the phase shift of the spins, which thus produces a better picture of the wave propagation.

MRE estimates the stiffness of the target tissue to track the evolution of a disease, to better understand the pathophysiology of the disease, to determine the most suitable therapy, and to evaluate long-term effects of treatment by monitoring gain of tissue function.

Thus, numerous experimental protocols associated with MRI and MRE techniques have been developed, based on the principle of applying a mechanical excitation to assess the shear modulus of healthy soft tissues (such as skeletal muscle: [BEN 07], [BRA 07], [CHA 15a], [DEB 11], [DRE 01], [KLA 10b]; brain: [GRE 08], [SAC 08]; heart: [ELG 10], [KOL 09]; liver: [KLA 10a], [LEC 13] kidney: [BEN 11]) and pathological organs (such as skeletal muscle: [BEN 07], [BEN 14]; fibrotic liver: [TER 18], [YIN 07]).

The MRE technique is composed of three main steps, allowing for the measurement of the shear modulus:

Step 1: Induce a mechanical deformation in the soft tissue

A speaker device driving the mechanical wave is located outside the MRI room to avoid interference. Two types of driver (pneumatic or mechanical) can be used to generate the waves at the surface of the biological tissue. These drivers must be carefully designed for MR compatibility to ensure a uniform wave displacement at a given frequency. Figure 5.1 (A-B) shows the round pneumatic driver (diameter: 16cm) used for the MRE liver test. The driver produced a uniform displacement of the membrane at frequencies ranging between 50Hz and 100Hz (Figure 5.1C) while a non-uniform generation of waves appeared at 110Hz (Figure 5.1D).

Step 2: Image the displacement of the shear wave

To spatially map and measure the wave displacement patterns, a phase-contrast MRI technique is used, in which a motion-sensitizing gradient (MSG) echo sequence is imposed along a specific direction and switched in polarity at an adjustable frequency [CAL 95], [DEN 93]. Trigger pulses

synchronize an oscillator unit that drives a transducer, coupled with the surface of the target tissue to be imaged, to induce shear waves in the tissue at the same frequency as the motion-sensitizing gradient.
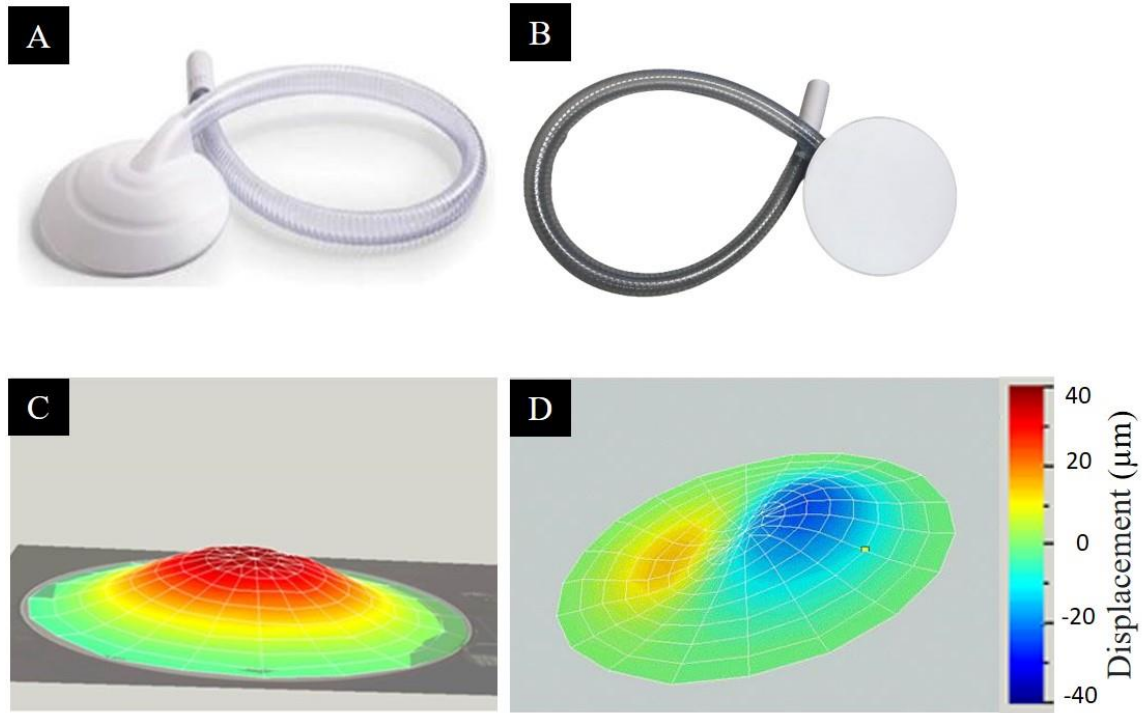

Figure 5.1. *Characterization of the amplitude of deformation, for the membrane of a pneumatic driver, as measured by a laser doppler vibrometer (modified from* [LEC 13])*. A and B: Pneumatic liver driver Resoundant[®], front and back view, respectively. C: Displacement of the membrane between 50Hz and 100Hz. D: Displacement of membrane at 110 Hz.*

During MRE imaging, any cyclic motion of the spins in the presence of these MSGs causes a measurable phase shift, φ, in the received MR signal. The displacement at each voxel is proportional to the measured phase shift, which is caused by a propagating mechanical wave with a wave vector $\vec{k}$, within a given medium, at a given frequency (f), in the presence of a cyclic MSG, and is given by:

$$\emptyset(\theta, \vec{r}) = \frac{\gamma NT (\vec{G_0} \cdot \vec{\varepsilon_0})}{2} \cos(\vec{k} \cdot \vec{r} + \theta) \qquad [1]$$

where $\emptyset$ is the phase shift (rad), $\vec{r}$ is the spin position vector, θ (rad) is the relative phase (offset) of the magnetic and mechanical oscillations, γ (rad·s^{-1}·T^{-1}) is the gyromagnetic ratio of the tissue proton, N is the number of gradient pairs used to sensitize the motion, T (s) is the period of the MSG (T=1/f), $\vec{G_0}$ is the MSG gradient vector and $\vec{\varepsilon_0}$ is the displacement amplitude vector [MUT 95], [MUT 96].

The accumulated phase shift is proportional to its displacement. The phase shift is also proportional to the period (*T*) of the MSG and the number (*N*) of gradient pairs. High sensitivity to small amplitude synchronous motion can be achieved by accumulating phase shifts over multiple cycles of mechanical oscillation and the MSG waveform.

Thus, the obtained MR images contains both the anatomical image and the propagating wave information (i.e. phase image), the latter of which is typically derived by collecting 2 images with opposite MEG polarities and calculating a phase-difference image (Figure 5.2).
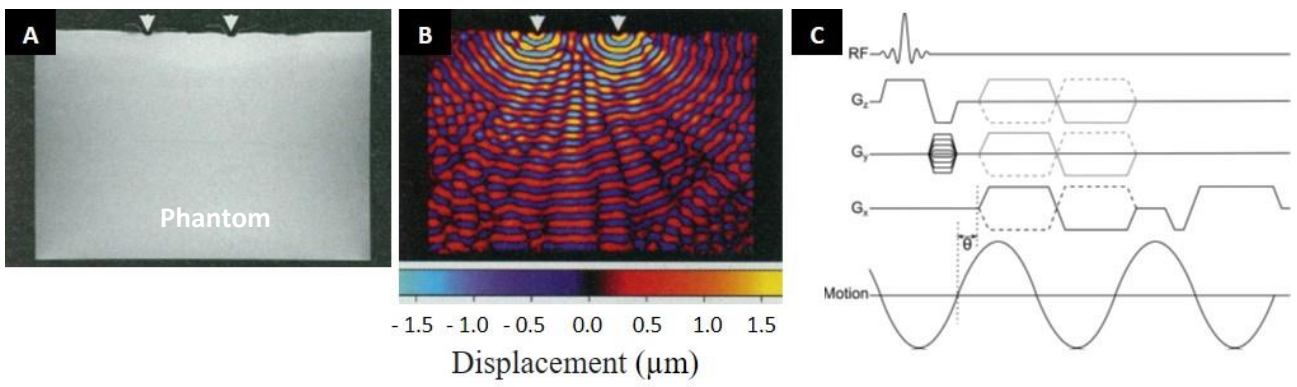
Figure 5.2. *Magnitude (A) and phase (B) images of an agarose gel phantom. (C) Spin Echo sequence (modified from [MUT 95]).*

Step 3: Measure the mechanical properties of the tissue

The mechanical properties can be locally or globally calculated using different methods:

- Local estimation of the shear modulus

From the phase image, the displacement of the waves is used to calculate the wavelength (λ). To accomplish this, a profile is manually drawn in the direction of the wave propagation to visualize the behavior of the wave (Figure 5.3B) and to measure the wavelength (Figure 5.3C).

Subsequently, assuming that the tissue is linear elastic, isotropic, homogeneous and incompressible, the local absolute shear modulus (μ) at a given oscillating frequency (f), called shear stiffness, is calculated using the following equation:

$$\mu = \rho. \, (f.\lambda)^2 \tag{2}$$

where ρ is the density of the biological tissue, fixed to 1000 kg.m^{-3} because the majority of the tissue content is made of water, and λ is the wavelength.

From the MRE displacement data (i.e. the phase image), it is possible to extract other mechanical properties, such as the complex shear modulus, using a variety of reconstruction techniques based on the equation of motion. The complex shear modulus (G*) is related to an elastic component (G'), that represents the real part, and a viscous component (G''), that represents the imaginary part. From the local profile drawn in the phase image, these two components can be calculated with the following equations at the angular frequency ($\omega = 2\pi f$) [CHA 15b]:

$$G'(\omega) = \rho\omega^2 \frac{(k^2 - \gamma^2)}{(k^2 - \gamma^2)^2 + (2k\gamma)^2} \tag{3}$$

$$G''(\omega) = \rho\omega^2 \frac{2k\gamma}{(k^2 - \gamma^2)^2 + (2k\gamma)^2} \tag{4}$$

where k is the real wave number ($k = 2\pi/\lambda$), and γ the attenuation coefficient.

- Cartography of the shear modulus

From the phase image, it is possible to generate a cartography of the shear modulus. This can be accomplished using different algorithms such as local frequency estimation (LFE) (Figure 5.3D), the matched filter (MF), phase gradient (PG), and direct inversion (DI) [MAN 96], [MAN 01].
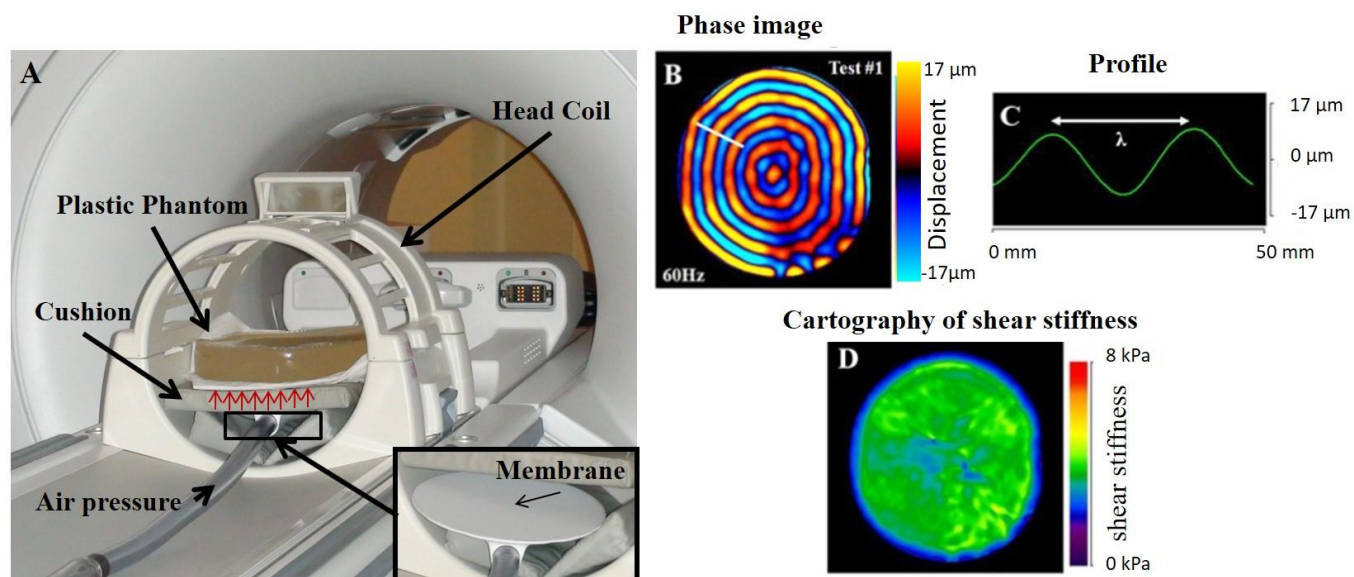
Figure 5.3. *(A) Experimental MRE set up for a phantom in plastisol. (B) Propagation of the shear waves inside the phantom with a profile line drawn in white (C) Behavior of the wave along the profile drawn from phase image. (D) Mapping of the shear stiffness obtained with the local frequency estimation (LFE) method (modified from* [LEC 13]).

6. Measurement of the lung shear modulus with MRE

Lung disease is one of the principal causes of death worldwide, from which four million people die annually [BOU 07]. Bacterial (staphylococcal pneumonia) and viral (ILD, COVID-19) lung diseases modify the mechanical behavior of the lung parenchyma, and the MRE technique can quantify differences in tissue stiffness to help determine the severity of the pathology. Table 6.1 shows the main studies that have used the MRE technique to assess the stiffness and density of the lungs at different conditions such as: breath hold at residual volume (RV), total lung capacity (TLC), midway between RV and TLC (MID), and free breathing [FAK 19], [FAK 22], [MARI 14], [MARIN 17].

Author	Measure	MR Sequence	MRI Machine	MRI and MRE Parameters
[FAK 22]	Shear stiffness	SE-EPI, 10 to 17 axial slices, Z direction, MEG (50 Hz)	Siemens 1.5T	Slice Thickness: 10 mm Repetition Time: 1020 ms Echo Time: 15 ms Imaging Frequency: 50 Hz Number of offsets: 4 Pixel size: 1.76 mm
[FAK 22]	Density	Fast GRE, 6 axial slices, Gadolinium-doped water phantom	Siemens 1.5T	Slice Thickness: 10 mm Repetition Time: 10 ms Echo Time: 0.98, 1.62, 2.26, and 2.9 ms (TLC) Number of averages: 4 Pixel size: 1.76 mm Correction factor: 1.736 or 1.782
[FAK 19]	Shear stiffness	SE-EPI, 5 axial slices, Z direction, MEG (50 Hz)	Siemens 1.5T	Slice Thickness: 10 mm Repetition Time: 400 ms Echo Time: 11.6 ms Echo train length: 10

				Imaging Frequency: 50 Hz Number of offsets: 4 Pixel size: 1.56 mm
[FAK 19]	Density	Fast GRE, 5 axial slices, Gadolinium-doped water phantom	Siemens 1.5T	Slice Thickness: 10 mm Repetition Time: 10 ms Echo Time: 1.07 ms and 1.5 ms (TLC) Number of averages: 4 Correction factor: 1.873 Pixel size: 1.56 mm
[MARIN 17]	Shear stiffness	SE-EPI, 4 axial slices, Z direction, MEG (50 Hz)	GE 1.5T	Slice Thickness: 15 mm Repetition Time: 320 ms Echo Time: 11.7 ms Echo train length: 10 Imaging Frequency: 50 Hz Number of offsets: 4 Pixel size: 3.75 mm
[MARIN 17]	Density	Fast GRE, 4 axial slices	GE 1.5T	Slice Thickness: 15 mm Repetition Time: 10 ms Echo Time: 1 ms and 1.8 ms (TLC) Flip angle: 10° Pixel size: 3.75 mm
[MARI 14]	Shear stiffness	SE-EPI, axial slices, Z direction, MEG (50 Hz)	GE 1.5T	Slice Thickness: 10 mm Repetition Time: 200 ms Echo Time: 9.4 ms Fractional Motion Encoding Imaging Frequency: 50 Hz Number of offsets: 4
[MARI 14]	Density	Fast GRE, 12 axial slices, Gadolinium-doped water phantom	GE 1.5T	Slice Thickness: 15 mm Repetition Time: 15 ms Echo Time: 1 ms and 1.8 ms (TLC) Flip angle: 10°

Table 6.1. *A literature survey of MRE and MRI techniques applied to human lungs.*

The right lung is usually analyzed to avoid the motion artifacts of the heart. As previously explained, the first step is to generate the shear wave inside the lung. For this, the pneumatic driver currently used for MRE liver testing is placed over the ribcage, anterior to the apex. An active acoustic driver (or speaker), connected with a plastic tube to the round driver, induces air pressure at 50Hz to deform the pneumatic membrane and induce the propagation of shear waves inside the lung [FAK 19], [MARI 14], [MARI 11] (Figure 6.1).
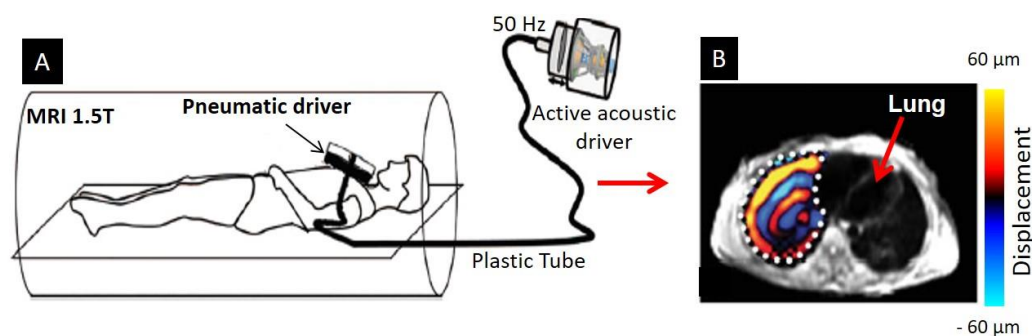

Figure 6.1. *A: Typical MRE setup for imaging the lung (modified from* [FAK 19]*. B: Phase image showing the displacement of the shear waves in the right lung (modified from* [MARI 14]*).*

Recently, the lung MRE set up has been further improved to assess the shear modulus of both lungs. In this process, an additional active acoustic driver is connected to two other smaller round pneumatic drivers placed on the left lung. Both speakers produce vibrations at 50 Hz [FAK 22] (Figure 6.2).
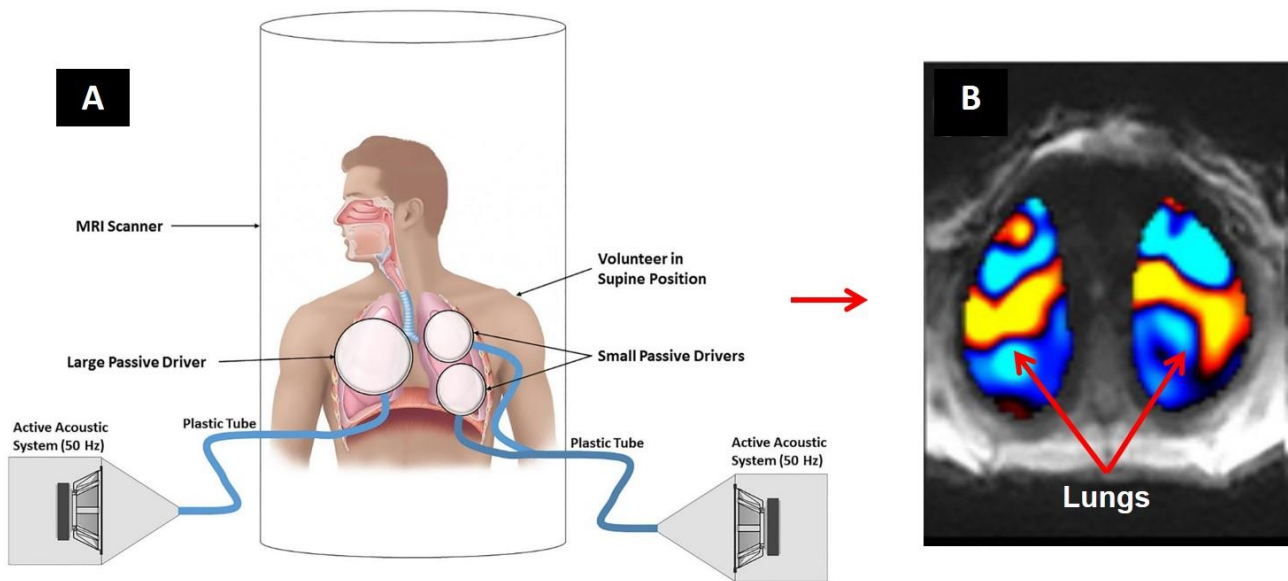

Figure 6.2. *A: Novel MRE set up for visualizing both lungs. B: Phase image showing the localization of the shear waves inside both lungs (modified from* [FAK 22]*).*

From the phase images obtained with both set ups, post-processing is performed as described in step 3. A mask is applied to left and right lungs to remove background noise, and a Butterworth directional filter is then applied to each image as well. A region of interest can be drawn on each magnitude (or anatomical) lung image, excluding major pulmonary arteries and veins, to analyze a specific area. Lung shear stiffness cartographies are obtained for each slice using 2D direct inversion for each encoding direction [FAK 19], [FAK 22], [MARI 14]. Then, a mean of all slices is assembled to obtain a single cartography of lung stiffness, from which one can calculate the pixel value of lung density, defined hereafter (Figure 6.3c).

Lung density can be estimated relative to the known density of a gadolinium-doped water phantom that is placed on the chest of the patients during the lung density scans (Figure 6.3a) [FAK 19], [MARI 14], [MARI 11], [HOL 11], [THE 09]. The accurate measurement of lung density is important for properly correcting the lung stiffness calculation [HOL 11], [THE 09]. The lung density map (Figure 6.3b) is computed on the basis of three steps:

1) Image acquisition of MR signal at 8 echo times t_j: $I_j = I_0 \exp(-t_j / T2^*)$ for determination of the initial signal I_0 and the relaxation time $T2^*$;

2) Calibration acquisition with gadolinium-doped water phantom for determination of a correction factor (CF) from MR acquisition at two repetition times (TR):

CF = (mean phantom signal at TR = 6 s) / (mean phantom signal at TR = 10 ms)

3) Calculation of lung density map (ρ):

$$\rho = \frac{I_0}{CF * I_{ph}}$$ [5]

where I_{ph} is the mean signal of the gadolinium-doped water phantom, CF the correction factor, and I_0 the mean signal of the phantom at echo time TE = 1 ms and TR = 10 ms [THE 09].

Marinelli et al. (2017) demonstrated an increase in shear stiffness for patients with interstitial lung disease (ILD), estimated at residual volume (RV) and total lung capacity (TLC) [MARIN 17]. Patients with ILD had a mean lung stiffness of 2.740 ± 0.896 kPa at TLC and 1.320 ± 0.300 kPa at RV, as compared with 1.330 ± 0.195 kPa at TLC and 0.849 ± 0.250 kPa at RV in healthy lungs.
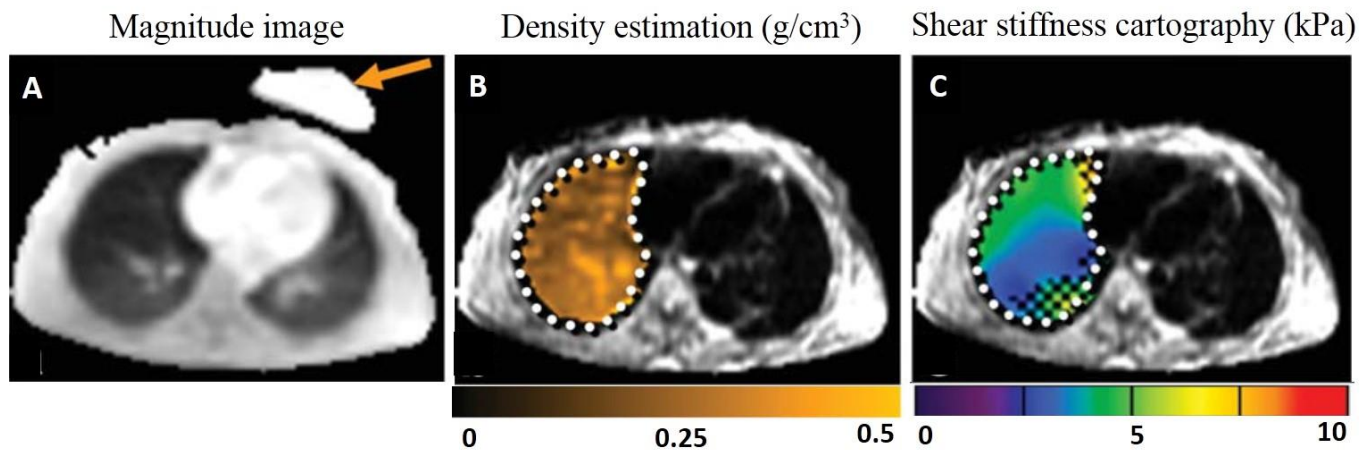

Figure 6.3. *Estimation of density. A: Mean MR magnitude images. B: Density map overlaid on the MRE magnitude image. C: Cartography of the shear stiffness obtained in ERM (modified from* [MARI 14]*).*

A comparison of the shear stiffness between the free-breathing and held breath conditions for the right and left lungs has been made [FAK 22]. The results show a difference of shear stiffness between free breathing and held breath for the right lung (mean difference: −0.65 kPa) and the left lung (mean difference: −0.75 kPa). Moreover, the free-breathing data in this study proved to be robustly repeatable and reproducible, demonstrating the feasibility of free-breathing lung MRE. In addition, this study identified no significant difference in lung stiffness between different age groups (20 to 40 years, n = 17, versus above 40 years, n = 8) or between genders (16 males and 9 females), and showed non-significantly higher (p = 0.14) stiffness values for the left lung compared to the right one. A significant difference in mean density of 0.05 g.cm^{-3} was observed between the right and left lung in both age groups.

7. Conclusion

To conclude, the association of MR techniques and CT scan (Figure 7.1) will provide subjective and quantitative data 1) to establish correlations between the shear stiffness and the morphological properties (lung volume, stage of fibrosis, etc.) for patients with different lung diseases, 2) to identify and follow up on the development of lung pathologies (ILD, post-COVID-19 fibrosis, etc.) and 3) to evaluate future anti-fibrosis therapies.
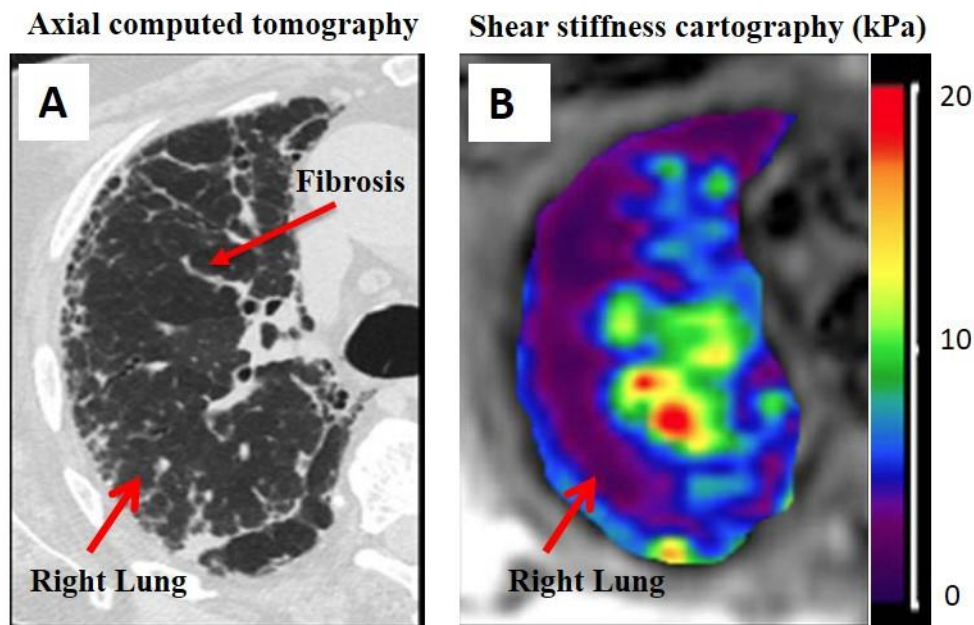
Figure 7. *A: Axial computed tomography (CT) of a lung with interstitial lung disease. B: Axial image cartography of the shear stiffness obtained from the same lung using MRE. Fibrosis areas have a higher shear stiffness, showing hardening of the tissue (modified from* [MARIN 17]).

Bibliography

[ATE 20] ATES O.F., TAYDAS O., DHEIR H. « Thorax Magnetic Resonance Imaging Findings in Patients with Coronavirus Disease (COVID-19) ». *Academic Radiology,* 27 (10), p. 1373-78, 2020.

[BEN 07] BENSAMOUN S.F., STACIE I.R, QINGSHAN C., RICHARD L.E., KAI-NAN AN., BRENNAN M. « Thigh Muscle Stiffness Assessed with Magnetic Resonance Elastography in Hyperthyroid Patients before and after Medical Treatment ». *Journal of Magnetic Resonance Imaging,* 26 (3), p. 708-13, 2007.

[BEN 11] BENSAMOUN S.F., ROBERT L., LECLERC E.G., DEBERNARD L., CHARLEUX F. « Stiffness Imaging of the Kidney and Adjacent Abdominal Tissues Measured Simultaneously Using Magnetic Resonance Elastography ». *Clinical Imaging,* 35 (4), p. 284-87, 2011.

[BEN 14] BENSAMOUN S.F. « Magnetic Resonance Elastography of the Skeletal Muscle ». In *Magnetic Resonance Elastography*, edited by Sudhakar K. Venkatesh and Richard L. Ehman, 81-87. Springer New York. http://link.springer.com/chapter/10.1007/978-1-4939-1575-0, 2014.

[BOU 07] BOUSQUET J., KHALTAEV N. « Global surveillance, prevention and control of chronic respiratory diseases: a comprehensive approach ». Geneva, Switzerland: World Health Organization (WHO), 2007.

[BRA 07] BRAUCK K., GALBAN C. J., MADERWALD S., HERRMANN B.L., LADD M.E. « Changes in Calf Muscle Elasticity in Hypogonadal Males before and after Testosterone Substitution as Monitored by Magnetic Resonance Elastography ». *European Journal of Endocrinology,* 156 (6), p. 673-78, 2007.

[BUR 16] BURGESS J.K., MAUAD T., TJIN G., KARLSSON C.J., THORSSON G.W. « The extracellular matrix – the under-recognized element in lung disease? » *The Journal of Pathology,* 240 (4), p. 397-409, 2016.

[CAL 95] CALLAGHAN P.T., STEPISNIK J. « Frequency-domain analysis of spin motion using modulated-gradient NMR ». *Journal of Magnetic Resonance, Series, A* 117 (1), p. 118-22, 1995.

[CHA 15a] CHAKOUCH M., CHARLEUX F., BENSAMOUN S.F. « Quantifying the Elastic Property of Nine Thigh Muscles Using Magnetic Resonance Elastography ». Édité par Carlos E. Ambrósio. *PLOS ONE,* 10 (9), e0138873. 2015.

[CHA 15b] CHAKOUCH M., POULETAUT P., CHARLEUX F., BENSAMOUN S.F. « Viscoelastic Shear Properties of in Vivo Thigh Muscles Measured by MR Elastography: Muscle Viscoelastic Properties Using MMRE ». *Journal of Magnetic Resonance Imaging,* 43 (6), p. 1423-33, 2015.

[CHAS 18] CHASSAGNON G., MARTIN C., BURGEL P., HUBERT D., FAJAC I., PARAGIOS N., ZACHARAKI E.I, LEGMANN P., COSTE J., REVEL M. « An automated computed tomography score for the cystic fibrosis lung ». *European Radiology,* 28 (12), p. 5111-20, 2018.

[DEB 11] DEBERNARD L., ROBERT L., CHARLEUX F., BENSAMOUN S.F. « Analysis of thigh muscle stiffness from childhood to adulthood using magnetic resonance elastography (MRE) technique ». *Clinical Biomechanics,* 26 (8), p. 836-40, 2011.

[DEN 93] DENK W., KEOLIAN R.M., OGAWA S., JELINSKI L. W. « Oscillatory Flow in the Cochlea Visualized by a Magnetic Resonance Imaging Technique. » *Proceedings of the National Academy of Sciences,* 90 (4), p. 1595-98, 1993.

[DIE 17] DIEFFENBACH P. B., HAEGER C. M., CORONATA A. M. F., MOO CHOI K, VARELAS X., TSCHUMPERLIN D. J., FREDENBURGH L. E. « Arterial stiffness induces remodeling phenotypes in pulmonary artery smooth muscle cells via YAP/TAZ-mediated repression of cyclooxygenase-2 ». *American Journal of Physiology-Lung Cellular and Molecular Physiology,* 313 (3), p. L628-47, 2017.

[DON 21] DONG D. I., TANG Z., WANG S., GONG H.H.L., LU Y., XUE Z. « The Role of Imaging in the Detection and Management of COVID-19: A Review ». *IEEE Reviews in Biomedical Engineering,* 14, p. 16-29, 2021.

[DRE 01] DRESNER A. M., ROSE G.H., ROSSMAN P.J., MUTHUPILLAI R., MANDUCA A., RICHARD L. E. « Magnetic resonance elastography of skeletal muscle ». *Journal of Magnetic Resonance Imaging,* 13 (2), p. 269-76, 2001.

[ELG 10] ELGETI T., BELING M., HAMM B., BRAUN J., SACK I. « Cardiac Magnetic Resonance Elastography: Toward the Diagnosis of Abnormal Myocardial Relaxation ». *Investigative Radiology,* 45 (12), p. 782-87, 2010.

[EHM 08] EHMAN E.C., ROSSMAN P.J., KRUSE S.A., SAHAKIAN A.V., GLASER K. J. « Vibration safety limits for magnetic resonance elastography ». *Physics in Medicine and Biology,* 53 (4), p. 925-35, 2008.

[FAF 09] FAFFE, D.S., ZIN W.A. « Lung Parenchymal Mechanics in Health and Disease ». *Physiological Reviews,* 89 (3), p. 759-75, 2009.

[FAK 19] FAKHOURI F., DONG H., KOLIPAKA A. « Magnetic Resonance Elastography of the Lungs: A Repeatability and Reproducibility Study ». *NMR in Biomedicine*, e4102. 2019.

[FAK 22] FAKHOURI F, KANNENGIESSER S., PFEUFFER J., GOKUN Y., KOLIPAKA A. « Free-breathing MR Elastography of the Lungs: An in Vivo Study ». *Magnetic Resonance in Medicine,* 87 (1), p. 236-48, 2022.

[FOW 95] FOWLKES J. B., EMELIANOV S. Y., PIPE J. G., SKOVORODA A. R., CARSON P. L., ADLER R. S., SARVAZYAN A. P. « Magnetic-resonance imaging techniques for detection of elasticity variation ». *Medical Physics,* 22 (11), p. 1771-78, 1995.

[GOS 06] GOSS B.C., MCGEE K.P., EHMAN E.C., MANDUCA A., EHMAN R.L. « Magnetic Resonance Elastography of the Lung: Technical Feasibility ». *Magnetic Resonance in Medicine,* 56 (5), p. 1060-66, 2006.

[GRE 08] GREEN M. A., BILSTON L.E., SINKUS R. « In Vivo Brain Viscoelastic Properties Measured by Magnetic Resonance Elastography ». *NMR in Biomedicine,* 21 (7), p. 755-64, 2008.

[GUA 20] GUAN W.J., WEI C.H., CHEN A.L., SUN X.C., GUO G.Y., ZOU.X., SHI J.D., LAI P.Z., ZHENG Z.G., ZHONG N.C. « Hydrogen/Oxygen Mixed Gas Inhalation Improves Disease Severity and Dyspnea in Patients with Coronavirus Disease 2019 in a Recent Multicenter, Open-Label Clinical Trial ». *Journal of Thoracic Disease,* 12 (6), p. 3448-52, 2020.

[HIR 13] HIROTA N., MARTIN.J.G. « Mechanisms of Airway Remodeling ». *Chest,* 144 (3), p. 1026-32, 2013.

[HOL 11] HOLVERDA S., THEILMANN R.J., SÁ R.C., ARAI T.J., HALL E.T., DUBOWITZ D.J., PRISK G.K., HOPKINS U.R. « Measuring Lung Water: Ex Vivo Validation of Multi-Image Gradient Echo MRI ». *Journal of Magnetic Resonance Imaging,* 34 (1), p. 220-24, 2011.

[JAN 99] JANSSENS J.P., PACHE J.C., NICOD L.P. « Physiological changes in respiratory function associated with ageing ». *European Respiratory Journal,* 13 (1), 197, 1999.

[KLA 10a] KLATT D., FRIEDRICH C., KORTH Y., VOGT R., BRAUN J, SACK I. « Viscoelastic properties of liver measured by oscillatory rheometry and multifrequency magnetic resonance elastography ». *Biorheology,* 47 (2), p. 133-41, 2010.

[KLA 10b] KLATT D., PAPAZOGLOU S., BRAUN J., SACK I. « Viscoelasticity-based MR elastography of skeletal muscle ». *Physics in Medicine and Biology,* 55 (21), p. 6445-59, 2010

[KOL 09] KOLIPAKA A., MCGEE K.P., PHILIP A. ARAOZ., KEVIN J. GLASER., ARMANDO MANDUCA., RICHARD L. EHMAN. « Evaluation of a Rapid, Multiphase MRE Sequence in a Heart-Simulating Phantom ». *Magnetic Resonance in Medicine,* 62 (3), p. 691-98, 2009.

[KOY 13] KOYAMA H., OHNO Y., SEKI S., NISHIO M., YOSHIKAWA T., MATSUMOTO S., SUGIMURA K. « Magnetic Resonance Imaging for Lung Cancer ». *Journal of Thoracic Imaging,* 28 (3), p. 138-50, 2013.

[LEC 13] LECLERC G.E., CHARLEUX F., ROBERT L., HO BA THO M.C, RHEIN C., LATRIVE J.P., BENSAMOUN S.F. « Analysis of liver viscosity behavior as a function of multifrequency magnetic resonance elastography (MMRE) postprocessing ». *Journal of Magnetic Resonance Imaging*, doi.org/10.1002/jmri.23986, 2013.

[LIUF 10] LIU F., MIH J.D., SHEA B.S., KHO A.T., SHARIF A.S., TAGER A.M., TSCHUMPERLIN D.J. « Feedback amplification of fibrosis through matrix stiffening and COX-2 suppression ». *Journal of Cell Biology,* 190 (4), p. 693-706, 2010.

[LIUW 20] LIU W., GUAN W.J., ZHONG N.S. « Strategies and Advances in Combating COVID-19 in China ». *Engineering,* 6 (10), p. 1076-84, 2020.

[MAN 96] MANDUCA A., MUTHUPILLAI R., ROSSMAN P.J., GREENLEAF J.F., EHMAN R.L. « Local wavelength estimation for magnetic resonance elastography ». In, *International Conference on Image Processing, Proceedings*, 3, p. 527-30, vol.3, 1996.

[MAN 01] MANDUCA A., OLIPHANT T.E., DRESNER M. A., MAHOWALD J. L., KRUSE S. A., AMROMIN E., FELMLEE J.P., GREENLEAF J.F., EHMAN R.L. « Magnetic resonance elastography: non-invasive mapping of tissue elasticity ». *Medical image analysis,* 5 (4), p. 237-54, 2001.

[MARI 11] MARIAPPAN Y.K., GLASER K.J., HUBMAYR R.D., MANDUCA A., EHMAN R.L., MCGEE K.P. « MR Elastography of Human Lung Parenchyma: Technical Development, Theoretical Modeling and in Vivo Validation ». *Journal of Magnetic Resonance Imaging,* 33 (6), p. 1351-61, 2011.

[MARI 14] MARIAPPAN Y.K., GLASER K.J., LEVIN D.L., VASSALLO R., HUBMAYR R.D., MOTTRAM C., EHMAN R.L., MCGEE K.P. « Estimation of the Absolute Shear Stiffness of Human Lung Parenchyma Using [1] H Spin Echo, Echo Planar MR Elastography: Lung EpiMRE ». *Journal of Magnetic Resonance Imaging,* 40 (5), p. 1230-37, 2014.

[MARIN 17] MARINELLI J.P., LEVIN D.L., VASSALLO R., CARTER R.E., HUBMAYR R.D., EHMAN R.L., MCGEE K.P. « Quantitative Assessment of Lung Stiffness in Patients with Interstitial Lung Disease Using MR Elastography: Quantifying Lung Stiffness in ILD ». *Journal of Magnetic Resonance Imaging,* 46 (2), p. 365-74, 2017.

[MUT 95] MUTHUPILLAI R., LOMAS D.J., ROSSMAN P.J., GREENLEAF J.F., MANDUCA A., EHMAN R.L. « Magnetic resonance elastography by direct visualization of propagating acoustic strain waves ». *Science,* 269 (5232), p. 1854-57, 1995.

[MUT 96] MUTHUPILLAI R., ROSSMAN P.J., LOMAS D.J., GREENLEAF J.F., RIEDERER S.J., EHMAN R.L. « Magnetic Resonance Imaging of Transverse Acoustic Strain Waves ». *Magnetic Resonance in Medicine,* 36 (2), p. 266-74, 1996.

[NOV 21] NOVAK C., BALLINGER M.N., GHADIALI S. « Mechanobiology of Pulmonary Diseases: A Review of Engineering Tools to Understand Lung Mechanotransduction ». *Journal of Biomechanical Engineering,* 143 (11), 110801, 2021.

[REV 05] REVEL M.P., PETROVER D., HERNIGOU A., LEFORT C., MEYER G., FRIJA G. « Diagnosing Pulmonary Embolism with Four–Detector Row Helical CT: Prospective Evaluation of 216 Outpatients and Inpatients ». *Radiology,* 234 (1), p. 265-73, 2005.

[SAC 08] SACK I., BEIERBACH B., HAMHABER U., KLATT D., BRAUN J. « Non-Invasive Measurement of Brain Viscoelasticity Using Magnetic Resonance Elastography ». *NMR in Biomedicine,* 21 (3), p. 265-71, 2008.

[SAR 14] SARRACANIE M., ARMSTRONG B.D., STOCKMANN J., ROSEN M.S. « High speed 3D overhauser-enhanced MRI using combined b-SSFP and compressed sensing ». *Magnetic Resonance in Medicine,* 71 (2), p. 735-45, 2014.

[SAR 15] SARRACANIE M., GREBENKOV D., SANDEAU J., COULIBALY S., MARTIN A.R., HILL K., SÁNCHEZ J.M.P. « Phase-Contrast Helium-3 MRI of Aerosol Deposition in Human Airways: PHASE-CONTRAST HELIUM-3 MRI OF AEROSOL DEPOSITION IN HUMAN AIRWAYS ». *NMR in Biomedicine,* 28 (2), p. 180-87, 2015.

[SHA 06] SHARMA G., GOODWIN J. « Effect of Aging on Respiratory System Physiology and Immunology ». *Clinical Interventions in Aging,* 1 (3), p. 253-60, 2006.

[SHI 20] SHI H., HAN X., ZHENG C. « Evolution of CT Manifestations in a Patient Recovered from 2019 Novel Coronavirus (2019-nCoV) Pneumonia in Wuhan, China ». *Radiology,* 295 (1), p. 20-20, 2020.

[SHIM 13] SHIMODA L.A., LAURIE S.S. « Vascular Remodeling in Pulmonary Hypertension ». *Journal of Molecular Medicine,* 91 (3), p. 297-309, 2013.

[SHK 15] SHKUMATOV A., THOMPSON M., CHOI K.M., SICARD D., BAEK K., KIM D.H., TSCHUMPERLIN D.J., PRAKASH Y. S., KONG H. « Matrix stiffness-modulated proliferation and secretory function of the airway smooth muscle cells ». *American Journal of Physiology-Lung Cellular and Molecular Physiology,* 308 (11), p. L1125-35, 2015.

[SIC 18] SICARD D., HAAK A.J., CHOI K.M., CRAIG A.R., FREDENBURGH L.E., TSCHUMPERLIN D.J. « Aging and Anatomical Variations in Lung Tissue Stiffness ». *American Journal of Physiology-Lung Cellular and Molecular Physiology,* 314 (6), p. L946-55, 2018.

[THE 09] THEILMANN R.J., ARAI T.J., SAMIEE A., DUBOWITZ D.J., HOPKINS S.R., BUXTON R.B, PRISK G.K. « Quantitative MRI Measurement of Lung Density Must Account for the Change in T_2^* with Lung Inflation ». *Journal of Magnetic Resonance Imaging,* 30 (3), p. 527-34, 2009.

[TOR 21] TORKIAN P., RAJEBI H., ZAMANI T., RAMEZANI N., KIANI P., AKHLAGHPOOR S. « Magnetic Resonance Imaging Features of Coronavirus Disease 2019 (COVID-19) Pneumonia: The First Preliminary Case Series ». *Clinical Imaging,* 69, p. 261-65, 2021.

[TER 18] TERNIFI R., POULETAUT P., SASSO M., MIETTE V., CHARLEUX F., BENSAMOUN S.F. « Improvements of Liver MR Imaging Clinical Protocols to Simultaneously Quantify Steatosis and Iron Overload ». *IRBM,* 39 (3), p. 219-25, 2018.

[WAN 20] WANG H., WEI R., RAO G., ZHU J., SONG B. « Characteristic CT findings distinguishing 2019 novel coronavirus disease (COVID-19) from influenza pneumonia ». *European Radiology,* 30 (9), p. 4910-17, 2020.

[YIN 07] YIN M., TALWALKAR J.A., GLASER K.J., MANDUCA A., GRIMM R.C., ROSSMAN P.J., FIDLER J.L., EHMAN R.L. « Assessment of Hepatic Fibrosis with Magnetic Resonance Elastography ». *Clinical Gastroenterology and Hepatology,* 5 (10), p. 1207-1213, e2, 2007.